

Mn-doped $\text{Bi}_{2-x}\text{Mn}_x\text{O}_3$ thin films: structural, optical, and dielectric properties for optoelectronic applications

Wael M. Mohammed¹, Fatemah H. Alkallas², Amira Ben Gouider Trabelsi², Mohamed S.I. Koubisy³, Ibrahim M. Sharaf³, and Abdelaziz M. Aboraia^{3,*}

¹ Physics Department, Faculty of Science, Minia University, P.O. Box 61519, Minia, Egypt

² Department of Physics, College of Science, Princess Nourah Bint Abdulrahman University, P.O. Box 84428, Riyadh 11671, Saudi Arabia

³ Physics Department, Faculty of Science, Al-Azhar University, Assiut Branch, Assiut 71524, Egypt

Received 12 September 2025 / Accepted 5 December 2025

Abstract. The current research investigates the influence of manganese (Mn) doping on the structural, optical, and dielectric properties of $\text{Bi}_{2-x}\text{Mn}_x\text{O}_3$ thin films for optoelectronic applications. The prepared thin films with different Mn content ($x = 0, 0.025, 0.05, 0.075, \text{ and } 0.1$) were synthesized, and their characteristics were thoroughly analyzed. Our findings demonstrate that increasing manganese content enhances light absorption by creating new electronic states, which is reflected in higher absorbance and lower transmittance values. The direct optical band gap decreases with higher Mn incorporation (from 3.60 eV for $x = 0$ –3.29 eV for $x = 0.1$), suggesting a tunable electronic structure. Furthermore, the Urbach energy increases with Mn concentration from 1.23 eV for $x = 0$ –3.33 eV for $x = 0.1$, indicating enhanced structural disorder and broadening of the band tail, which can benefit photovoltaic applications. Analysis of refractive index, extinction coefficient, and dielectric parameters ($\epsilon_1, \epsilon_2, \text{ and } \text{Tan}\delta$) demonstrates improved optical density, dielectric polarization, and reduced dielectric losses with Mn doping. These results establish clear correlations between Mn concentration and the resulting physical properties, providing crucial insights for optimizing Bi_2O_3 -based materials for high-performance optoelectronic applications.

Keywords: Optical properties, Absorbance, Bandgap narrowing, Electronic transitions, Refractive index, Photocatalysis.

1 Introduction

Understanding semiconductor materials' structural, optical, and dielectric properties, especially when they are made into thin films, is crucial because these materials play a key role in today's electronic and optoelectronic devices [1–4]. Among various metal oxides, bismuth oxide (Bi_2O_3) is distinguished by its advantageous characteristics, including a high refractive index, significant dielectric permittivity, a wide optical band gap, and notable photoconductivity [5, 6]. Thanks to these properties, Bi_2O_3 thin films show great promise for various uses, including optical coatings, gas sensors, photocatalytic systems, and other optoelectronic components [5, 7].

However, the intrinsic properties of pure Bi_2O_3 may not always fulfill the precise requirements for advanced device applications [8, 9]. Modifying these properties through

controlled doping with suitable elements presents a well-established and effective strategy [9]. The introduction of dopant ions into the host lattice can significantly alter the crystal structure of the material, defect chemistry, electronic band structure, and, consequently, its optical and electrical behavior [10, 11]. Manganese (Mn) is a particularly intriguing dopant for Bi_2O_3 , given the differences in ionic radius and valence state between Mn^{2+} and Bi^{3+} [12, 13]. Incorporating Mn is anticipated to induce lattice strain, modify defect concentrations (such as oxygen vacancies for charge compensation), and alter the electronic density of states, thereby offering a pathway to tune the material's functional properties for optoelectronic applications precisely [14, 15].

While numerous studies have explored the properties of pure and doped Bi_2O_3 systems, a comprehensive and systematic investigation into the influence of varying Mn ratios on the correlated structural, optical, and dielectric characteristics of $\text{Bi}_{2-x}\text{Mn}_x\text{O}_3$ films is highly warranted. Understanding how parameters such as crystallite size,

* Corresponding author: a.m.aboraia@gmail.com;
a.m.aboraia@azhar.edu.eg

microstrain, optical band gap, Urbach energy, extinction coefficient, refractive index, and dielectric complex evolve with Mn content is critical for optimizing these materials for targeted optoelectronic device applications. In this context, both Wenting D. and Congshan Z. [16] and Yanfei C. et al. [17] have studied the direct absorption band gap (Eg) of Bi₂O₃, finding consistent results that bulk Bi₂O₃ is a direct semiconductor with a band gap around 2.85 eV. When synthesized as Stearic acid-coated nanoparticles, a blue shift occurs, increasing the band gap – orange Bi₂O₃ nanoparticles exhibit a band gap near 3.33 eV (0.48 eV blue shift), and wine-red ones near 3.28 eV (0.43 eV blue shift). This increase is mainly attributed to the quantum confinement effect, which alters the electronic structure due to reduced particle size and surface effects. Although Yanfei C. et al. focused on band gap and luminescence, their results corroborate these band gap trends. These findings highlight the significant impact of nanoparticle size and surface modification on Bi₂O₃'s optical and electronic properties, underscoring the importance of studying how Mn doping similarly influences these parameters to enhance optoelectronic performance.

Therefore, the present work focuses on systematically characterizing Bi_{2-x}Mn_xO₃ thin films with varying Mn contents ($x = 0, 0.025, 0.050, 0.075, \text{ and } 0.1$). We investigate the structural modifications using X-ray diffraction (XRD). Detailed optical properties are analyzed based on UV-Vis-NIR spectroscopy measurements (absorbance, transmittance, reflectance) to determine the optical parameters (absorption coefficient – optical band gap – Urbach energy – refractive index – extinction coefficient) and dispersion parameters via the Wemple-DiDomenico model. Furthermore, the dielectric properties ($\epsilon_1, \epsilon_2, \text{ and } \text{Tan}\delta$) are evaluated to understand the films' response to electric fields. The aim is to establish clear correlations between the Mn doping level and the resulting physical properties, providing invaluable insights for the fabrication of high-performance Bi₂O₃-based optoelectronic devices.

2 Experimental methods

For this investigation, all necessary chemical reagents, including isopropanol, citric acetate, and bismuth oxide, were procured from Sigma Aldrich. Bi_{2-x}Mn_xO₃ nanoparticles, with “ x ” values ranging from 0 to 0.1, were synthesized via a sol-gel combustion technique. This process commenced with the dissolution of manganese nitrate, bismuth oxide, and citric acid in 50 ml of isopropanol within a beaker. The blend was continuously stirred at normal temperature to ensure stoichiometric proportions of citric acid and metal cations. Subsequent heating to 150 °C with a magnetic stirrer facilitated solvent evaporation and gel formation. Further heating ignited the gel, producing a significant flame, and the resulting material was then heated to 600 °C before being finely ground. The gel-combustion method was selected for its simplicity, cost-effectiveness, and high efficiency, aligning with circular economy principles through sustainable resource utilization [18]. To prepare films, the synthesized Bi₂O₃:Mn powder was

combined with a Chitosan solution at optimized concentrations. Uniform and high-performing films were achieved by a 1-hour dip-coating period at an extraction rate of 40 mm/min. post-deposition, the films underwent annealing at 300 °C in a nitrogen atmosphere, with a controlled temperature ramp of 0.2 °C/min, to preserve structural integrity and mitigate thermal stress. The film thickness of the materials which calculated according to the ref. [19]. The crystalline structures of both pure Bi₂O₃ and Bi₂O₃:Mn powders were meticulously analyzed using a LAscientific X-ray diffraction (XRD) machine equipped with Cu K α radiation ($\lambda = 1.54 \text{ \AA}$). Microstructural characterization was performed using a Supra (Zeiss) FE-SEM (Field emission scanning electron microscope) operating at 15.0 kV. Finally, the optical bandgap and transmission spectra of the prepared samples were investigated utilizing a Jasco V670 instrument.

3 Results and discussion

Figure 1a exhibits the XRD analysis plotted as intensity (arbitrary units, a.u.) versus the diffraction angle 2θ in degrees of Bi_{2-x}Mn_xO₃. All samples exhibit well-defined diffraction peaks, indicating crystalline structures. The peak positions and intensities vary slightly across the samples, reflecting changes in composition. The primary diffraction peaks are located at specific 2θ values, which correspond to characteristic reflections from the crystal lattice. The most prominent peaks appear around $2\theta = 28^\circ, 34^\circ, 46^\circ, \text{ and } 57^\circ$, and confirmed Bi₂O₃ is a monoclinic phase with COD No. 96-152-6459 [20]. As the Mn concentration decreases (from Bi_{1.90}Mn_{0.10}O₃ to Bi₂O₃), the overall peak intensities tend to decrease. The Bi₂O₃ sample (black curve) shows the lowest peak intensities, suggesting a less crystalline or more amorphous structure compared to the other samples. The patterns for Bi_{1.90}Mn_{0.10}O₃ to Bi_{1.975}Mn_{0.025}O₃ are consistent with perovskite-like structures, as evidenced by the sharp and well-defined peaks. The Bi₂O₃ sample displays broadened diffraction peaks, suggestive of diminished crystallinity or the potential presence of secondary crystalline phases. Increasing Mn content (x in Bi_{2-x}Mn_xO₃) leads to subtle shifts in peak positions, likely due to lattice parameter variations caused by Mn substitution. The peak broadening observed in the Bi₂O₃ sample suggests that the absence of Mn results in a less ordered crystal structure. The elemental analysis confirmed that the pure material was Bi₂O₃ and the doping with Mn was successful, as shown in Figure S1 (a-f).

The peak positions in the XRD patterns were used to further analyze the structural evolution caused by Mn doping. A systematic shift of the diffraction peaks to lower 2θ values was observed with increasing Mn content (x) in Bi_{2-x}Mn_xO₃, as illustrated in Figure 1b. According to Bragg's law, a decrease in the diffraction angle (2θ) corresponds to an increase in the interplanar spacing (d). This lattice expansion suggests that the incorporated Mn ions are effectively modifying the host lattice. The expansion could be due to the ionic radius difference between the host cation (Bi³⁺) and the dopant, or it may be driven by the

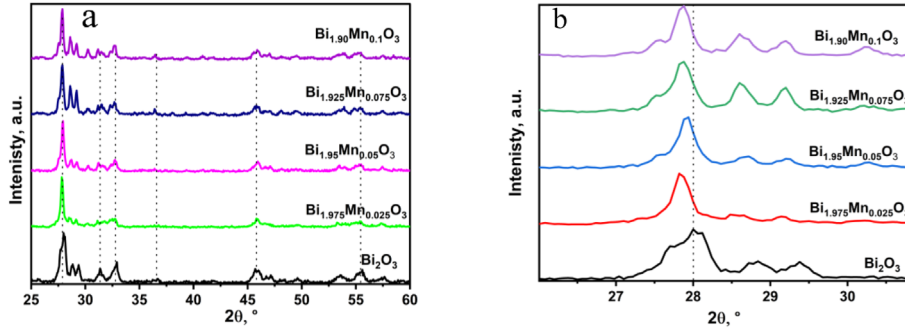


Figure 1. Characterization of $\text{Bi}_{1-x}\text{Mn}_x\text{O}_3$ thin films. (a) Full-range XRD patterns show a dominant preferred orientation. (b) A close-up of the primary peak region (27° – 30°) shows a constant shift in the 2θ position, indicating a change in the out-of-plane lattice parameter due to the incorporation of varying amounts of Mn.

formation of oxygen vacancies to maintain charge balance, a common phenomenon in such oxide systems. The average crystallite size and lattice strain of the synthesized $\text{Bi}_{2-x}\text{Mn}_x\text{O}_3$ powders were determined using the Williamson-Hall (W-H) analysis. This method is based on the principle that the broadening of X-ray diffraction (XRD) peaks is caused by two main factors: (1) the finite size of the crystallites (size broadening), and (2) lattice distortions due to imperfections such as dislocations, point defects, or dopant-induced strain (strain broadening). The total broadening (β_{total}) is expressed as a linear combination:

$$\beta_{\text{total}} = \beta_{\text{size}} + \beta_{\text{strain}}, \quad (1)$$

where β_{size} is related to the crystallite size (D) by the Scherrer equation, and β_{strain} is proportional to the strain (ϵ). This relationship is formulated in the following equation, known as the uniform deformation model (UDM) of the W-H plot:

$$\beta_{\text{hkl}} \cos \theta = (K\lambda / D) + 4\epsilon \sin \theta. \quad (2)$$

Here, β_{hkl} is the full width at half maximum (FWHM in radians) of a specific ($h k l$) reflection, θ is the Bragg angle, K is the Scherrer constant (a shape factor, ~ 0.9), λ is the X-ray wavelength, D is the volume-weighted average crystallite size, and ϵ is the effective microstrain.

The influence of manganese doping on the structural parameters of $\text{Bi}_{2-x}\text{Mn}_x\text{O}_3$, as determined from X-ray diffraction line broadening analysis, is summarized in [Table 1](#). A remarkable reduction in crystallite size by an order of magnitude is observed with the introduction of a small amount of Mn ($x = 0.025$), decreasing from ~ 1633 nm for the pristine sample ($x = 0$) to ~ 88 nm. This suggests that Mn doping effectively inhibits crystallite growth. As the doping level increases further ($x = 0.05$ to $x = 0.1$), the crystallite size does not follow a simple trend, fluctuating between 247 nm and 617 nm, which may indicate complex changes in the nucleation and growth dynamics. Concurrently, the microstrain within the crystals shows a general increasing trend with higher Mn content. The lowest strain (0.00315) is found for $x = 0.025$, while the highest (0.0093) is for $x = 0.1$. This inverse correlation between crystallite size and strain is a common phenomenon in doped materials, where lattice distortions

Table 1. The calculated crystalline size and strain of $\text{Bi}_{2-x}\text{Mn}_x\text{O}_3$.

| $\text{Bi}_{2-x}\text{Mn}_x\text{O}_3$ | Crystalline size, nm | Strain, ϵ |
|--|----------------------|--------------------|
| $X = 0$ | 1632.50883 | 0.00798 |
| $X = 0.025$ | 88.28025 | 0.00315 |
| $X = 0.05$ | 246.61922 | 0.0064 |
| $X = 0.075$ | 616 | 0.0088 |
| $X = 0.1$ | 541.40625 | 0.0093 |

induced by the dopant ions lead to increased internal strain, particularly at higher concentrations.

The FESEM images in [Figure 2](#) exhibit how the surface of $\text{Bi}_{2-x}\text{Mn}_x\text{O}_3$ thin films changes with different amounts of manganese added. When the Mn concentration is low (image a), the surface looks smooth and dense, suggesting that the grains have grown uniformly with very few defects. This type of surface typically results in fewer grain boundaries and greater crystal clarity, which can enhance the electrical and magnetic properties of the material. As the Mn content causing the observed porosity, and instead link the morphological changes to the inhibitory effect of Mn doping on crystal growth and its promotion of agglomerate formation. On the hand of the surface porosity and the grain size, the substitution of smaller Mn ions for Bi ions induces lattice strain, causing the increase in grain size and surface porosity seen at the highest Mn doping level. This strain disrupts crystal development, encouraging grain merging to form larger grains, which lowers the strain energy. The strain also results in internal voids and flaws that manifest as elevated porosity and surface roughness. This explains the morphological changes detected by FE-SEM. These changes in surface texture can affect how well the material conducts electricity and responds magnetically. Overall, the SEM images show how adding Mn changes the film's structure, which is important when designing these materials for electronics or spintronics applications.

The connection between a material's absorbance and wavelength provides insights into its electronic structure, with spectral peaks indicating electronic transitions that

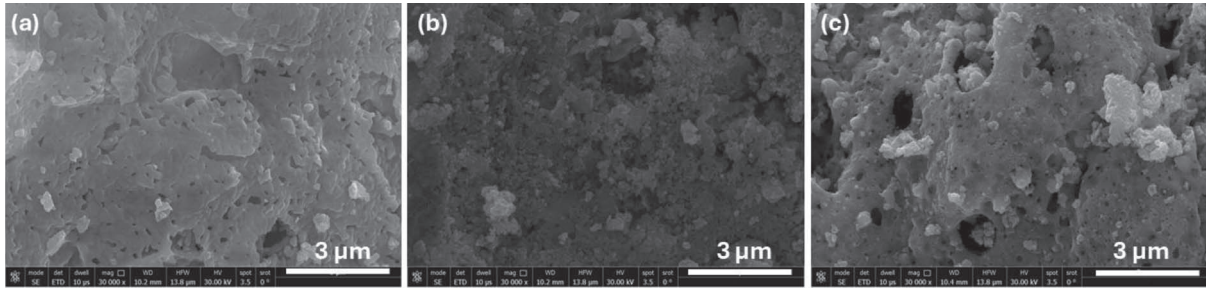


Figure 2. FESEM photos of (a) Bi_2O_3 , (b) $\text{Bi}_{1.95}\text{Mn}_{0.05}\text{O}_3$, and (c) $\text{Bi}_{1.9}\text{Mn}_{0.1}\text{O}_3$. The scale bars show a length of 3 μm for reference.

reveal molecular behavior [21, 22]. Figure 3 illustrates the absorbance-wavelength relationship for pure $\text{Bi}_{2-x}\text{Mn}_x\text{O}_3$ thin films ($x = 0$) and those doped with different Mn contents ($x = 0, 0.025, 0.05, 0.1$). Higher Mn concentrations rise absorbance, suggesting improved light absorption due to new electronic states within the material's bandgap. Additionally, absorbance peak amplitudes rise with increased Mn content, indicating stronger or more probable electronic transitions. Substituting Mn for Bi may introduce defects or traps in the crystal lattice, facilitating these transitions. Incorporating Mn could alter the Bi_2O_3 lattice's electronic structure by modifying valence and conduction bands or introducing localized states, enhancing absorption properties. A narrowed bandgap may shift the absorption spectra toward the red. Elevated Mn concentrations could enhance photocatalytic properties, making the material more effective for applications like photocatalysis or solar energy harvesting, as the enhanced absorbance in the visible spectrum suggests improved light-harvesting capabilities [23, 24].

Understanding and designing optical devices necessitates understanding thin film transmittance and reflectance. Transmittance indicates the amount of light passing through the film, while reflectance shows the portion reflected. These properties, influenced by the film's thickness and material composition, can be tailored to control light interaction at specific wavelengths. Figures 4a and 4b illustrate the wavelength-dependent transmittance and reflectance, respectively. In Figure 4a, increasing Mn concentration in Bi_2O_3 thin films reduces transmittance, likely due to enhanced light absorption or scattering caused by Mn. This suggests that Mn introduces new energy levels or defects in the Bi_2O_3 structure, increasing absorption and reducing light transmission. Higher Mn levels also amplify certain electronic transition peaks, possibly due to localized states that enhance transition probabilities [25]. In Figure 4b, reflectance rises with raised Mn content, likely due to changes in the material's refractive index from doping. Higher Mn content may increase scattering at internal or external surfaces, leading to greater light reflection. These optical property changes enable the customization of thin films for applications like photocatalytic systems, where precise light control is essential, or optoelectronic devices, where tailored absorption and reflection are critical. Such modifications highlight the potential of Mn-doped Bi_2O_3 films for advanced optical and energy-related technologies.

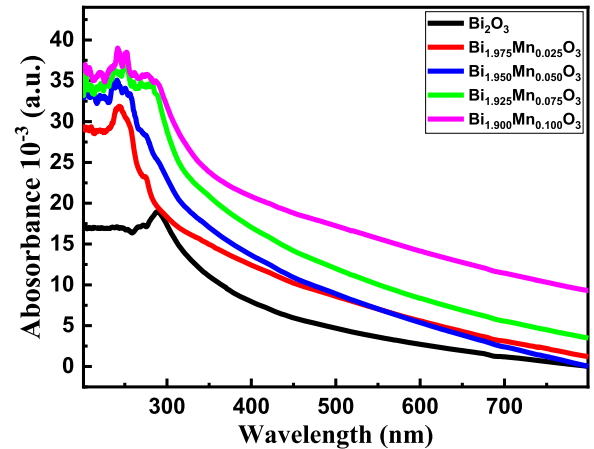


Figure 3. Wavelength dependence of absorbance for the $\text{Bi}_{2-x}\text{Mn}_x\text{O}_3$ thin films.

Analyzing the absorption coefficient (α) of a material is crucial for elucidating its composition and structure, which is vital for developing optical devices such as lenses, solar cells, and filters. The absorption coefficient is calculated based on the material's transmittance (T) and reflectance (R) values, as outlined in references [26, 27].

$$\alpha = \frac{1}{d} \ln \left[\frac{(1 - R)^2 + [(1 - R)^4 + 4R^2 T^2]^{1/2}}{2T} \right]. \quad (3)$$

Where d is the thickness of the thin films. Figure 5, which displays the absorption coefficient versus the energy of photons, shows that increasing the Mn content enhances the ability of the material to absorb the light. This improvement is likely due to Mn doping creating new energy levels within the bandgap, facilitating easier electronic transitions upon light exposure. As expected for semiconductor materials, the absorption coefficient generally increases with higher photon energy. Additionally, a sharp peak observed in Figure 5 points to resonant transitions. This peak's intensity slightly increases as the Mn content rises (from $x = 0$ to $x = 0.1$), suggesting a higher density of available electronic states at greater Mn concentrations, which enhances the probability of photon absorption at those specific energies. The peaks also shift and broaden with increased Mn doping, which is related to the changes in the Bi_2O_3 electronic structure induced by the doping. A possible explanation involves

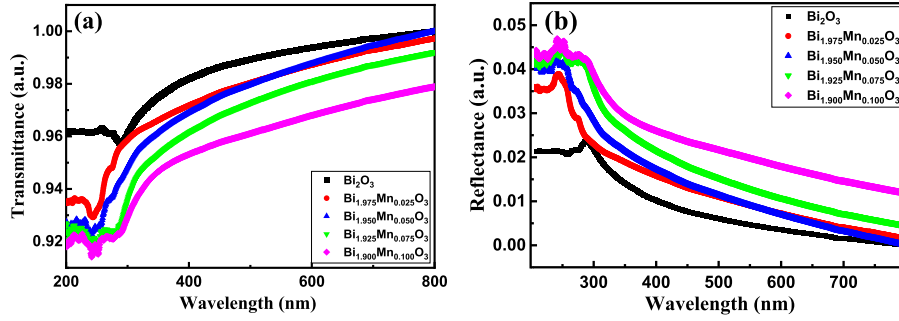


Figure 4. (a) Transmittance and (b) reflectance as a function of wavelength for the $\text{Bi}_{2-x}\text{Mn}_x\text{O}_3$ thin films.

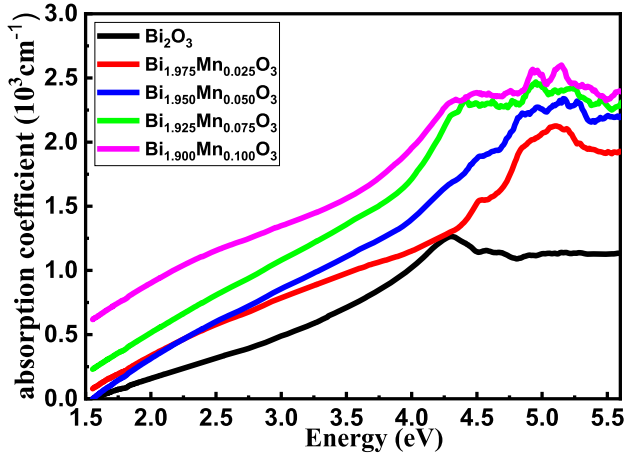


Figure 5. Absorbance coefficient for the $\text{Bi}_{2-x}\text{Mn}_x\text{O}_3$.

the creation of localized energy states that modify the band structure, thereby reducing the energy required for particular electronic transitions to occur.

The Urbach tail, corresponds to photon energies below the bandgap, indicates structural disorder in thin-film semiconductors, related to localized states [28]. The established empirical approach can be applied to calculate the Urbach energy in the low energy region, as detailed in references [29–31].

$$\alpha(\nu) = \alpha_0 \exp\left(\frac{h\nu}{E_u}\right). \quad (4)$$

The symbols ν , h , α_0 , and α denote the frequency, Planck’s constant, a material-specific constant, and the absorption coefficient, respectively. Equation (2) is expressed as follows:

$$\ln(\alpha(\nu)) = \ln(\alpha_0) + \frac{1}{E_u} h\nu. \quad (5)$$

By analyzing the slope of the relationship between photon energy and $\ln(\alpha)$ (Fig. 6a), the Urbach energy values were calculated. As exhibited in Figure 6b, the Urbach energy rises with higher Mn concentrations. This can be attributed to significant alterations in the electronic properties due to increased Mn content, which modifies the band structure and broadens the band tail, elevating the Urbach energy. The Williamson–Hall analysis (Table 1) indicates that the

$x = 0.1$ sample exhibits the highest microstrain ($\epsilon = 0.0093$) in the series, reflecting a pronounced lattice distortion that generates band-tail states through the formation of localized energy levels within the band gap. This effect is further intensified by the considerable reduction in crystallite size from approximately 1633 nm ($x = 0$) to about 541 nm ($x = 0.1$), which significantly increases the grain boundary area. These boundaries represent disordered regions rich in suspended bonds and defects, leading to a higher density of intra-gap states and a consequent broadening of the band tails. Morphological observations from the FESEM images (Fig. 2c) support these findings, as the $x = 0.1$ sample displays a rough, porous surface with evident structural flaws, directly illustrating the increased disorder at this doping level. Moreover, the incorporation of Mn ions at high concentrations introduces substantial electronic disorder through charge compensation mechanisms – such as the formation of oxygen vacancies – and localized lattice distortions around the dopant sites, collectively contributing to the pronounced tailing of the band edges. Similar behavior was observed in S_xWO_3 , where higher S content correlated with increased Urbach energy [29].

Additionally, the optical energy gap (E_g^{opt}) for $\text{Bi}_{2-x}\text{Mn}_x\text{O}_3$ thin films at the high absorption edge was calculated by the Tauc formula [30] as follows:

$$\alpha h\nu = B\left(h\nu - E_g^{\text{opt}}\right)^A. \quad (6)$$

Here, B represents the Tauc parameter, and A is a constant. Semiconductors can facilitate optical transitions either directly or indirectly [31]. Equation (4) can be written as:

$$\begin{aligned} \sqrt[A]{\alpha h\nu} &= \sqrt[A]{B} \times \left(h\nu - E_g^{\text{opt}}\right) \text{ Or; } \sqrt[A]{\alpha h\nu} \\ &= \sqrt[A]{B} \cdot h\nu - \sqrt[A]{B} \cdot E_g^{\text{opt}}. \end{aligned} \quad (7)$$

Equation (5) shows the straight-line relation between $\sqrt[A]{\alpha h\nu}$ and $h\nu$. The optical band gap (E_g^{opt}) is determined from the x -axis intercept of the extrapolated line as follows:

$$\begin{aligned} \text{At} \\ \sqrt[A]{\alpha h\nu} = 0 &\Rightarrow \sqrt[A]{B} \cdot h\nu = \sqrt[A]{B} \cdot E_g^{\text{opt}} \Rightarrow h\nu = E_g^{\text{opt}}. \end{aligned} \quad (8)$$

Now, to determine the direct and the indirect allowed transition, this can be obtained using the constant A . The value of “ A ” depends on the nature of the electronic transition

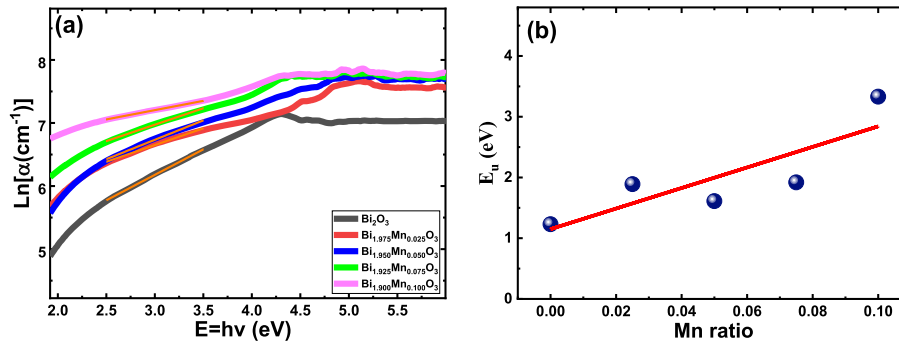


Figure 6. (a) Dependency of $\ln(\alpha)$ with photon energy for $\text{Bi}_{2-x}\text{Mn}_x\text{O}_3$ thin films, (b) urbach energy vs Mn concentration.

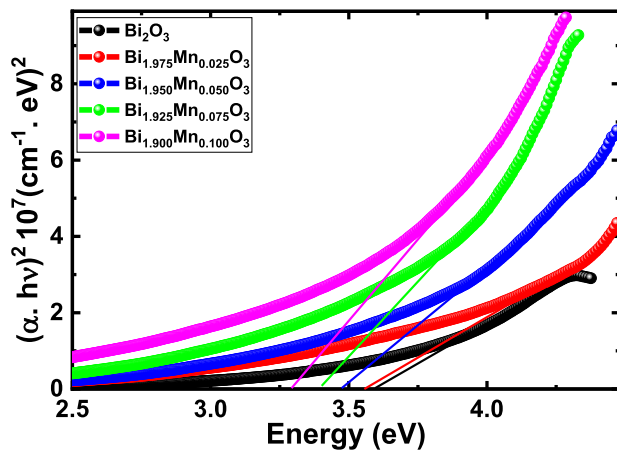


Figure 7. The direct energy gap for the $\text{Bi}_{2-x}\text{Mn}_x\text{O}_3$ thin films.

that occurs when the material absorbs a photon. For the most common types of transitions, the direct allowed transitions which $A = \frac{1}{2}$ and the indirect allowed transitions which $A = 2$. The $h\nu$ dependence of $(\alpha h\nu)^2$ is plotted in Figure 7. The data presented in the Figure indicates that the linear part of $(\alpha h\nu)^2$ plot versus $(h\nu)$ exhibits a clearer linearity. This finding implies that a direct electronic transition predominates in the thin films under investigation. This was observed in a previous study for Co-doped ZnO thin films [32]. The calculated values of the direct band gap energy (E_g^{opt}) are listed in Table 2. The reduction in the direct energy band gap of $\text{Bi}_{2-x}\text{Mn}_x\text{O}_3$ thin films with increasing Mn content is primarily due to the introducing of Mn-3d states, which modify the electronic structure through hybridization with O-2p orbitals and/or the creation of defect-related energy levels. Structural changes and charge compensation mechanisms may also contribute [33, 34]. This band gap narrowing suggests that Mn doping can be used to tailor the optical and electronic properties of Bi_2O_3 for specific applications, such as photocatalysis or photovoltaic devices, where a reduced band gap enhances performance under visible light.

The observed increase in the extinction coefficient (K) of $\text{Bi}_{2-x}\text{Mn}_x\text{O}_3$ thin films with increasing Mn content ($x = 0$ to 0.1) and the corresponding enhancement of the

peak at approximately 280 nm suggest a stronger absorption of light, likely due to the embedding of Mn into the Bi_2O_3 lattice, as shown in Figure 8. This increase in K indicates a higher probability of photon absorption, which can be attributed to the introduction of Mn-3d electronic states that enhance the material's interaction with incident light, particularly in the ultraviolet region [33]. The peak at 280 nm, which intensifies with higher Mn content, likely corresponds to an electronic transition involving these Mn-related states or defect levels, such as charge transfer between Mn and O orbitals, aligning with the previously noted band gap reduction from 3.6 eV to 3.29 eV. This enhanced absorption and peak intensity with increasing Mn doping suggests improved optical activity, potentially making the material more effective for applications like photocatalysis, as the additional Mn-induced states facilitate greater light harvesting in the UV spectrum.

Analysis of a material's refractive index (n) is crucial for determining the local electric field and electronic polarization of its constituent atoms or ions. The refractive index is typically determined by measuring the transmittance (T) and reflectance (R) spectra, as established in previous studies [18].

$$n = \left(\frac{(1+R)}{(1-R)} \right) + \left(\left(\frac{(1+R)}{(1-R)} \right)^2 - k^2 + 1 \right)^{0.5} \quad (9)$$

Figure 9a illustrates the wavelength-dependent refractive index of $\text{Bi}_{2-x}\text{Mn}_x\text{O}_3$ thin films. The increased Mn content elevates the refractive index, attributed to modifications in the electronic and structural properties of the material, enhancing its optical performance. This improvement is promising for applications in light manipulation and advanced optical devices. The refractive index values, measured across a wavelength range of 200–1000 nm, align closely with the Cauchy formula [35]. Additional optical properties were derived from these refractive index values, with dispersion parameters proving essential for optimizing optical communication systems and spectral dispersion control devices. A comprehensive understanding of the films' optical behavior requires detailed knowledge of the single oscillator energy (E_0) and dispersion energy (E_d), which are related to photon energy ($h\nu$) through the Wemple-DiDomenico model [36].

Table 2. Bi_{2-x}Mn_xO₃ thin-film optical parameter changes.

| Sample | Direct E_q^{Opt} (eV) | E_u (eV) | E_d (eV) | E_0 (eV) | f | n_0 | ϵ_∞ | $S_0 \times 10^{12}$ (m ²) | λ_0 (nm) | $N/m^* \times 10^{55}$ (m ⁻³ kg ⁻¹) | ϵ_L |
|-------------|----------------------------|---------------|---------------|---------------|-------|-------|-------------------|---|---------------------|---|--------------|
| $X = 0$ | 3.60 | 1.23 | 1.81 | 5.34 | 9.67 | 1.16 | 1.34 | 5.18 | 244 | 9.75 | 1.56 |
| $X = 0.025$ | 3.56 | 1.89 | 3.49 | 6.67 | 23.28 | 1.23 | 1.52 | 11.22 | 206 | 12.2 | 1.77 |
| $X = 0.05$ | 3.47 | 1.61 | 3.13 | 6.01 | 18.81 | 1.24 | 1.53 | 9.8 | 220 | 14.4 | 1.82 |
| $X = 0.075$ | 3.40 | 1.92 | 3.71 | 6.12 | 22.71 | 1.27 | 1.61 | 12.4 | 214 | 12.6 | 1.89 |
| $X = 0.1$ | 3.29 | 3.33 | 4.45 | 6.41 | 28.52 | 1.30 | 1.69 | 19.1 | 192 | 98.2 | 2.01 |

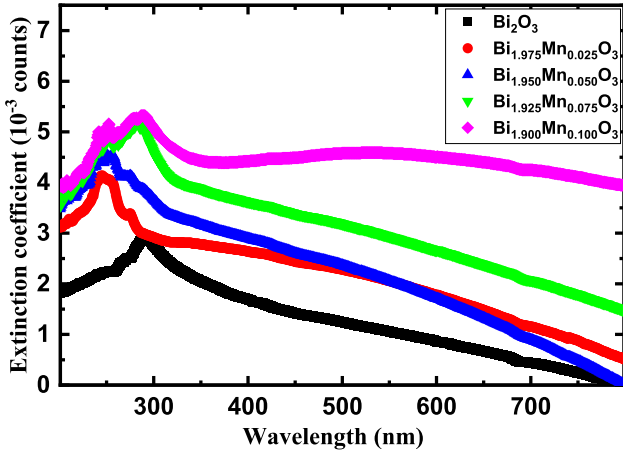


Figure 8. Extinction Coefficients versus wavelength for Bi_{2-x}Mn_xO₃ thin films.

$$(n^2 - 1)^{-1} = \frac{E_0^2 - (hv)^2}{E_0 E_d} = \frac{E_0}{E_d} - \frac{(hv)^2}{E_0 E_d} \Rightarrow (n^2 - 1)^{-1} = \frac{E_0}{E_d} - \frac{1}{E_0 E_d} (hv)^2. \quad (10)$$

The parameters E_0 and E_d were determined through a graphical analysis of $(n^2 - 1)^{-1}$ vs $(hv)^2$, as presented in Figure 8b. Table 2 systematically lists the values of E_0 and E_d . The lattice dielectric constant (ϵ_∞) and static refractive index (n_0) were calculated using a formula dependent on the constants E_0 and E_d [37].

$$\epsilon_\infty = \frac{E_d + E_0}{E_0} \quad \text{and} \quad n_0 = \sqrt{\frac{E_d + E_0}{E_0}}. \quad (11)$$

Table 2 reveals that the calculated values of both n_0 and ϵ_∞ increase with a higher Mn content, indicating enhanced optical density and dielectric polarization in the investigated thin films due to Mn incorporation. Additionally, the oscillator strength of the material, calculated as $[f = E_d \times E_0]$, was determined using the parameters E_0 and E_d and is reported in Table 2. The Sellmeier dispersion model was utilized to calculate the resonance wavelength (λ_0) and oscillator strength (s_0) at lower frequencies. This model is essential for elucidating the interaction of light with the material across various wavelengths. Its efficacy at lower frequencies highlights its suitability for analyzing optical properties [38].

$$(n^2 - 1)^{-1} = (s_0 \lambda_0^2)^{-1} - \left(\frac{1}{s_0}\right) (\lambda)^{-2}. \quad (12)$$

Figure 9c illustrates the determination of λ_0 and s_0 values through linear fitting of $1/(n^2 - 1)$ versus $1/\lambda^2$, with the resulting values reported in Table 2. The lattice dielectric constant (ϵ_L) quantifies the material's response to an applied electric field at low frequencies, reflecting its capacity to store electrical energy as polarization [39, 40]. The term (N/m^*), representing the charge carrier contribution to the refractive index, indicates that the refractive index of the material changes with increasing carrier density or decreasing effective mass. Consequently, accurate measurement of ϵ_L and $\frac{N}{m^*}$ is essential for characterizing the investigated thin films. Figure 8d depicts the relationship between n^2 and λ^2 , from which ϵ_L and $\frac{N}{m^*}$ are derived using equation (11) [41].

$$n^2 = \epsilon_L - \left(\frac{e^2}{4\pi^2 c^2 \epsilon_0}\right) \left(\frac{N}{m^*}\right) \lambda^2. \quad (13)$$

The obtained values of ϵ_L and $\frac{N}{m^*}$ are listed in Table 2. The observed increase in both the lattice dielectric constant (ϵ_L) and the charge carrier contribution to the refractive index ($\frac{N}{m^*}$) with higher Mn content indicates that the optical and electronic properties of Bi_{2-x}Mn_xO₃ thin films are increasingly conducive to polarization and charge transport. This enhancement suggests potential for improved performance in optoelectronic applications.

The transport properties, grain structure, and grain boundary behavior of compounds can be analyzed through the dielectric loss (ϵ_2) and dielectric constant (ϵ_1). Additionally, the dielectric constant provides insight into a material's capacity to store electrical energy [42–47]. These parameters also characterize the response of the material to both optical and electric fields. The real component (ϵ_1) governs the refractive index and phase velocity of light within the medium, whereas the imaginary component (ϵ_2) relates to absorption, indicating the extent of light attenuation by the material. The real and imaginary components of the complex permittivity of the thin films can be derived using the following expressions, respectively [25]:

$$\epsilon_1 = n^2 - k^2, \quad (14)$$

$$\epsilon_2 = 2nk. \quad (15)$$

Figures 10a and 10b present the spectral dependence of the real (ϵ_1) and imaginary (ϵ_2) dielectric constants,

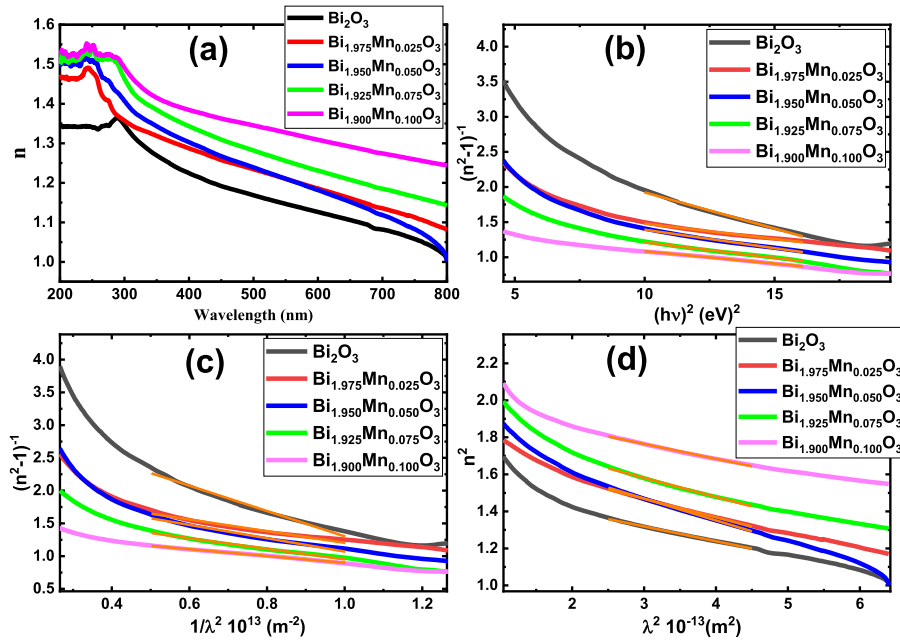


Figure 9. The deduced values involve: (a) refractive index variation with λ , (b) variation of $(n^2 - 1)^{-1}$ with $(hv)^2$ to estimate E_0 and E_d , (c) the relation between $(n^2 - 1)^{-1}$ and $(1/\lambda^2)$ for obtaining S_0 and λ_0 , and (d) λ^2 dependence of n^2 to calculate ε_L and $\frac{N}{m^3}$ for $\text{Bi}_{2-x}\text{Mn}_x\text{O}_3$ thin films for different Mn concentrations.

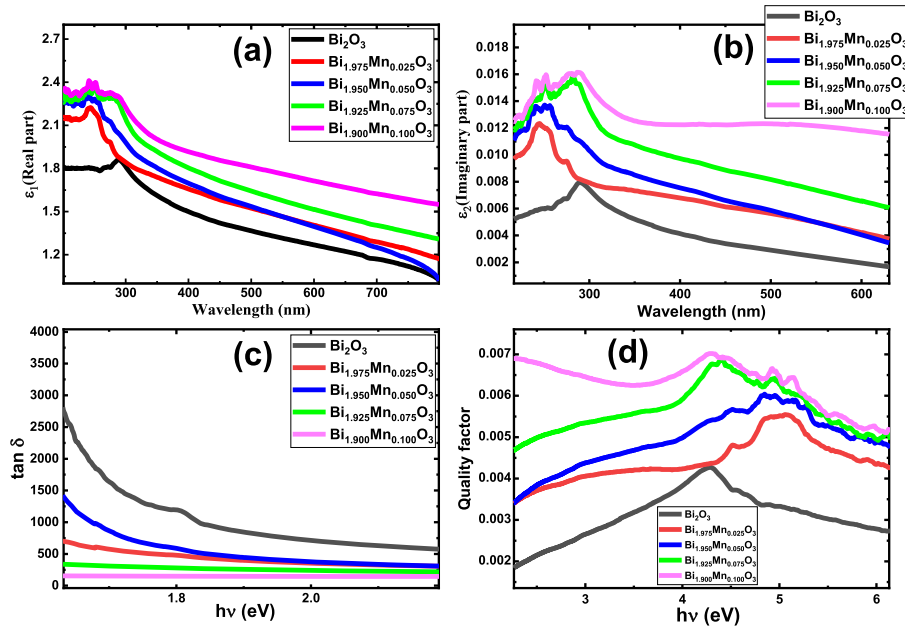


Figure 10. Dielectric constant (a) and dielectric loss (b) vs wavelength, and loss tangent (c) and quality factor (d) vs hv $\text{Bi}_{2-x}\text{Mn}_x\text{O}_3$ thin films.

respectively. The rise in ε_1 with increasing Mn content indicates enhanced dielectric polarization, likely due to the introduction of additional dipoles that strengthen the material's dielectric response. Similarly, ε_2 exhibits an increase with higher Mn concentrations, suggesting a greater contribution from energy dissipation mechanisms. The loss tangent ($\tan\delta$) can be expressed by the following relation [48]:

$$\text{Tan}(\delta) = \frac{\varepsilon_2}{\varepsilon_1}. \quad (16)$$

Figure 10c illustrates the dependence of the loss tangent ($\text{Tan} \delta$) on photon energy for the investigated thin films. A decrease in $\text{Tan} \delta$ was observed with increasing Mn content, attributed to alterations in the electronic energy levels

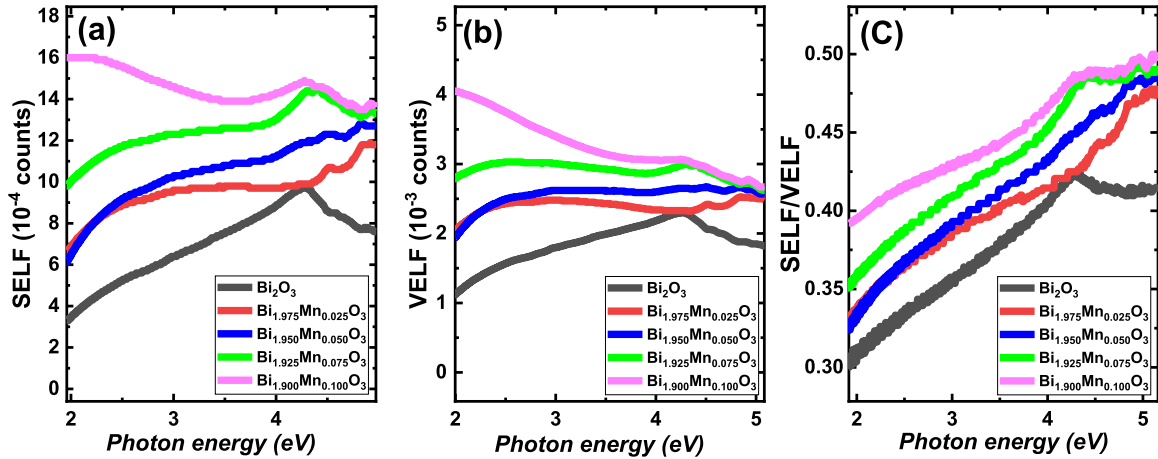


Figure 11. The variation of (a) SELF, (b) VELF, and (c) (SELF/VELF) with vs $h\nu$ for $\text{Bi}_{2-x}\text{Mn}_x\text{O}_3$.

resulting from Mn incorporation. The quality factor (Q -factor), which quantifies a material's ability to store and release energy, is depicted in Figure 10d as a function of photon energy ($h\nu$) for $\text{Bi}_{2-x}\text{Mn}_x\text{O}_3$ thin films. As photon energy increases, the Q -factor rises, indicating improved energy storage or reduced energy dissipation. This suggests enhanced energy efficiency and lower dielectric losses at higher photon energies. At the high frequencies, materials with low-loss dielectric responses typically exhibit less pronounced energy dissipation, a trend corroborated by the measured behavior of the real and imaginary components of the dielectric constant.

The characterization of electron transitions in thin films relies on two crucial parameters: the Surface Energy Loss Function (SELF) and the Volume Energy Loss Function (VELF) [36, 49, 50]. The ratio of SELF to VELF describes these electron transitions across both low and high energy ranges within the examined thin film [36]. For the current films, SELF and VELF can be calculated using a specific equation [50], with the results illustrated in Figures 10a and 10b.

$$\text{SELF} = \frac{\varepsilon_2}{(\varepsilon_1 + 1)^2 + \varepsilon_2^2}, \quad (17)$$

$$\text{VELF} = \frac{\varepsilon_2}{\varepsilon_1^2 + \varepsilon_2^2}. \quad (18)$$

From Figures 11a, 11b, it is observed that both SELF and VELF values rise with an increasing Mn content. This is associated with changes in electron transition energy due to the incorporation of Mn into the thin films. Figure 11c illustrates the ratio of SELF/VELF against photon energy, indicating that the addition of Mn affects the electron transitions within the films.

An essential measure for understanding the electronic characteristics of thin films is the optical (σ_{Opt}) and electrical conductivity (σ_{elec}), which is closely connected to the dielectric properties that describe how the materials interact with radiation. Using the values of the parameters α , n , and λ , the following relations can be used to generate σ_{Opt} and σ_{elec} [51, 52]:

$$\sigma_{\text{Opt}} = \frac{\alpha n c}{4\pi} \quad \text{and} \quad \sigma_{\text{elec}} = \frac{\lambda n c}{2\pi}. \quad (19)$$

The wavelength, the absorption coefficient, the refractive index, and the speed of light are denoted by λ , α , n , and c . The variation of σ_{Opt} and σ_{elec} of the $\text{Bi}_{2-x}\text{Mn}_x\text{O}_3$ thin-film with the wavelength is intr in Figures 12a and 12b. As the Mn content rises, it is noticed that both σ_{Opt} and σ_{elec} increase as well; the maximum optical and electrical conductivity was achieved for the highest Mn content. This could be ascribed to the modifications made to the thin films' electrical structure as a result of adding Mn. Also, this is related to the enhanced absorption coefficient due to the doping with Mn [53]. The degree of polarization is closely correlated with the electric susceptibility for any polarizable material. The material's electric susceptibility quantifies how easily it polarizes when subjected to an electric field. A material with a high electric susceptibility will polarise more significantly in an electric field, which in turn reduces the net electric field within the material. The Electric susceptibility (χ_c) can be found using the following expression [51]:

$$\chi_c = \frac{1}{4\pi} [n^2 - K^2 - n_0^2]. \quad (20)$$

The equation includes n , K , and n_0 parameters which represent the thin film's refractive index, extinction coefficient, and the index of refraction for the surroundings, respectively. As illustrated in Figure 12c, the electric susceptibility χ_c increases proportionally with the Mn-to-Bi content in the film. This trend arises because Mn incorporation modifies the electronic band structure, altering the material's interaction with applied electric fields. Additionally, the disparity in polarizability between Mn and Zn ions enhances χ_c as Mn content increases, as polarizability directly influences charge distribution under external fields.

The nonlinear refractive index (n_2) and the linear (χ^1) and nonlinear (χ^3) susceptibilities of a material are expressed as follows [54]:

$$\chi^{(1)} = \frac{E_d/E_0}{4\pi}, \quad (21)$$

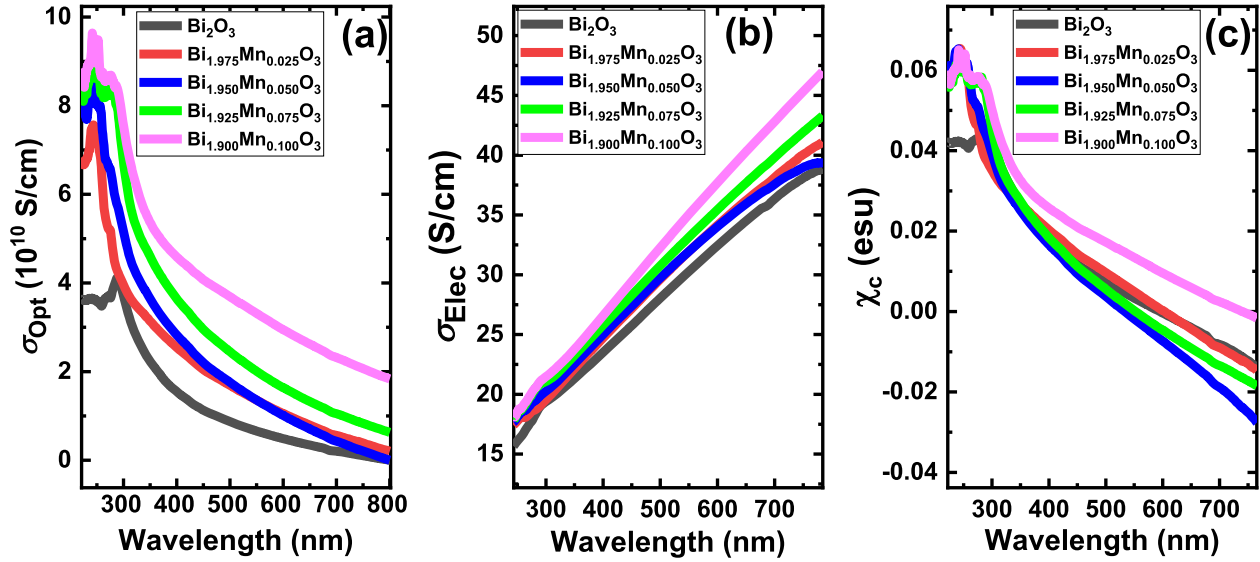


Figure 12. Plotting of (a) the optical conductivity and (b) the electrical susceptibility vs wavelength for $\text{Bi}_{2-x}\text{Mn}_x\text{O}_3$ thin films.

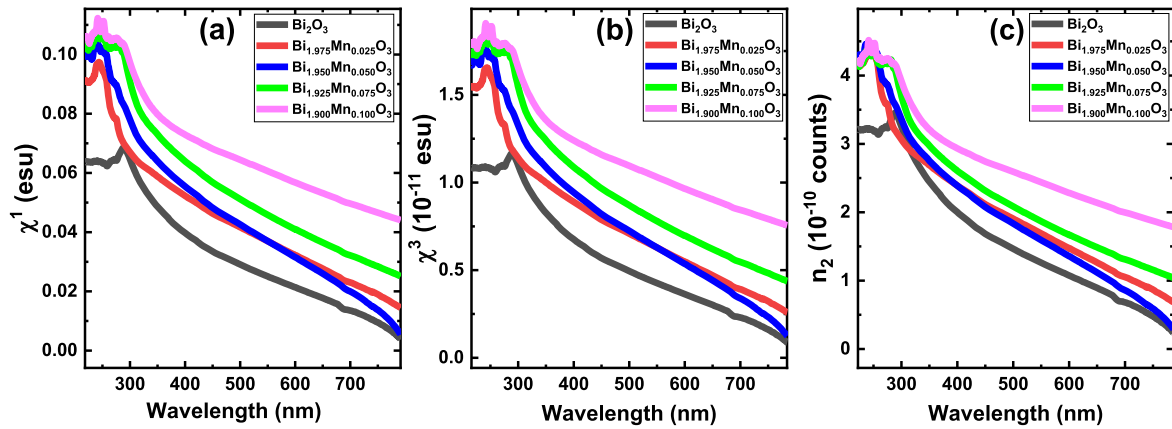


Figure 13. The variation of the linear (a) and the non-linear susceptibility (b) and non-linear refractive index with λ for $\text{Bi}_{2-x}\text{Mn}_x\text{O}_3$ thin films.

$$\chi^{(3)} = \left(\frac{E_d}{E_0}\right)^4 \times (6.82 \times 10^{-15})(e.s.u.), \quad (22)$$

$$n_2 = \frac{12\pi\chi^{(3)}}{n_0}. \quad (23)$$

Figures 13a–13c depict the wavelength-dependent behavior of the nonlinear refractive index (n_2), linear susceptibility (χ^1), and nonlinear susceptibility (χ^3) for $\text{Bi}_{2-x}\text{Mn}_x\text{O}_3$ thin films, respectively. These parameters consistently increase with higher Mn content, reflecting changes in polarizability and electronic structure induced by Mn incorporation [55]. The enhanced optical properties of these films are highly beneficial for various applications. Precise control over nonlinear optical characteristics facilitates efficient frequency conversion and optical limiting, critical for advanced photonic and optoelectronic systems.

A comprehensive understanding of these modifications is essential for the rational design and development of next-generation materials tailored for cutting-edge optical technologies [2, 56].

Figure 14 exhibits the variation of the nonlinear absorption coefficient (β_c) and the energy for the $\text{Bi}_{2-x}\text{Mn}_x\text{O}_3$ thin films. The maximum value of β_c shifts towards a lower energy photon as the concentration of Mn rises. Doping Mn can establish additional energy levels inside the band gap. Because electrons can be excited from these confined states into the conduction band, these mid-gap states can help absorb lower-energy photons. Since additional photon energies are now resonant with these states, the nonlinear absorption coefficient increases at lower energy. Two-photon absorption and saturable absorption are two of the optical processes that affect the nonlinear absorption coefficient. The density of states varies with increasing Mn content, changing the way these processes take place.

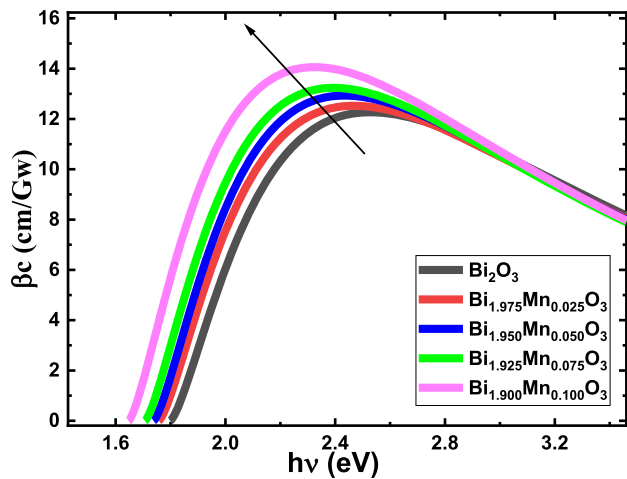


Figure 14. The dependency of the non-linear absorption coefficient on $h\nu$ for $\text{Bi}_{2-x}\text{Mn}_x\text{O}_3$ thin films.

Increased nonlinear absorption at lower energies could result from stronger interactions between photons and bound electron-hole pairs or exciton states.

4 Conclusion

This study highlights the significant influence of Mn doping on the structural, electronic, and optical properties of $\text{Bi}_{2-x}\text{Mn}_x\text{O}_3$ thin films. Increasing Mn concentration ($x = 0$ to 0.1) enhances absorbance, reduces transmittance, and increases reflectance, indicating improved light absorption due to the introduction of new electronic states within the bandgap. The absorption coefficient rises with higher Mn content, accompanied by a sharp peak and a shift in absorption spectra, suggesting enhanced electronic transitions and a narrowed bandgap from 3.6 eV to 3.29 eV. The Urbach energy increases with Mn doping, reflecting greater structural disorder and localized states, which further supports the observed optical enhancements. The refractive index, dielectric constants, and optical and electrical conductivities also increase with Mn incorporation, driven by modifications in the electronic structure and enhanced polarization. These changes, coupled with increased nonlinear optical properties such as the nonlinear refractive index and absorption coefficient, demonstrate the potential of Mn-doped Bi_2O_3 thin films for tailoring optical behavior. The findings suggest that precise control of Mn doping is critical for optimizing the performance of $\text{Bi}_{2-x}\text{Mn}_x\text{O}_3$ thin films in applications such as photocatalysis, photovoltaic devices, and advanced optoelectronic systems.

Funding

The authors express their gratitude to Princess Nourah bint Abdulrahman University Researchers Supporting Project number (PNURSP2025R38), Princess Nourah bint Abdulrahman University, Riyadh, Saudi Arabia.

Conflicts of interest

The authors declare no conflict of interest.

Data availability statement

The datasets used and/or analyzed during the current study are available from the corresponding author on reasonable request.

Author contribution statement

Conceptualization: Wael Mohammed and A.M. Aboraia; Methodology: Ibrahim M. Sharaf; Software, Validation: Amira Ben Gouider Trabelsi, Fatemah H. Alkallas, and Mohamed S.I. Koubisy; Formal Analysis: Mohamed S.I. Koubisy; Investigation: Ibrahim M. Sharaf; Writing – Original Draft Preparation: Fatemah H. Alkallas, Mohamed S.I. Koubisy; Writing – Review & Editing: Fatemah H. Alkallas and A.M. Aboraia; Visualization: Ibrahim M. Sharaf; Supervision: Abdelaziz M. Aboraia; Funding Acquisition: Fatemah H. Alkallas.

Supplementary material

Figure S1: The EDS of pure Bi_2O_3 and doping with different concentrations of Mn.

The supplementary material of this article is available at <https://jeos.edpsciences.org/10.1051/jeos/2025054/olm>.

References

- Buckley D, Lonergan A, O'Dwyer C, Review – ZnO-based thin film metal oxide semiconductors and structures: transistors, optoelectronic devices and future sustainable electronics, *ECS J. Solid State Sci. Technol.* **14**(1), 015001 (2025).
- Virt I, Recent advances in semiconducting thin films, *Coatings* **13**(1), 79 (2023).
- Haggren T, Tan HH, Jagadish C, III–V thin films for flexible, cost-effective, and emerging applications in optoelectronics and photonics, *Acc. Mater. Res.* **4**(12), 1046–1056 (2023).
- AlAbdulaal T, et al., Investigating the structural morphology, linear/nonlinear optical characteristics of Nd_2O_3 doped PVA polymeric composite films: Kramers-Kronig approach, *Phys. Scr.* **96**(12), 125831 (2021).
- Mane V, et al., A review on Bi_2O_3 nanomaterial for photocatalytic and antibacterial applications, *Chem. Phys. Impact.* **8**, 100517 (2024).
- Leontie L, *Photoconductivity characteristics of bismuth oxide in thin films*. 12-th National Conference of the Romanian Physical Society (2002).
- Condurache-Bota S, Bismuth oxide thin films for optoelectronic and humidity sensing applications, *Bismuth-Adv. Appl. Defects Character.* 171–204 (2018). <https://doi.org/10.5772/intechopen.71174>.
- Maeder T, Review of Bi_2O_3 based glasses for electronics and related applications, *Int. Mater. Rev.* **58**(1), 3–40 (2013).
- Ghaedi M, *Photocatalysis: fundamental processes and applications*, , **Vol. 32** (Academic Press, Elsevier, UK).
- Costa MB, et al., Current trending and beyond for solar-driven water splitting reaction on WO_3 photoanodes, *J. Energy Chem.* **73**, 88–113 (2022).
- Sabolsky EM, et al., Doping effects on multivalence states, electronic structure, and optical band gap in LaCrO_3 under varied atmospheres: An integrated experimental and density

- functional theory study, *ACS Appl. Electron. Mater.* **7**(6), 2515–2528 (2025).
- 12 Kayani ZN, et al., Synthesis and investigation; influence of Mn doping on biological, optical, dielectric and electrochemical characteristics of Bi₂O₄ nanostructures, *Mater. Chem. Phys.* **314**, 128869 (2024).
 - 13 Khan AuR, et al., Structural, optical, electrical and photocatalytic investigation of *n*-Type Zn²⁺-doped α -Bi₂O₃ nanoparticles for optoelectronics applications, *ACS Omega*. **9**(21), 22650–22659 (2024).
 - 14 Uzair M, et al., Effect of Mn doped on structural, optical, and dielectric properties of BiFe_{1-x}Mn_xO₃ for efficient antioxidant activity, *ACS Omega*. **8**(45), 42390–42397 (2023).
 - 15 Wang S, et al., Bi/Mn-doped BiOCl nanosheets self-assembled microspheres toward optimized photocatalytic performance, *Nanomaterials* **13**(17), 2408 (2023).
 - 16 Dong W, Zhu C, Optical properties of surface-modified Bi₂O₃ nanoparticles, *J. Phys. Chem. Solids*. **64**(2), 265–271 (2003).
 - 17 Chen Y, et al., A study of nonlinear optical properties in Bi₂O₃-WO₃-TeO₂ glasses, *J. Non-Cryst. Solids* **354**(29), 3468–3472 (2008).
 - 18 Aboraia AM, et al., Exploration of the structural rGO thin films and their optical characteristics for optoelectronic device applications, *J. Optics* **54**, 1714–1723 (2024).
 - 19 Crawford LJ, Edmonds NR, Calculation of film thickness for dip coated antireflective films, *Thin Solid Films*. **515**(3), 907–910 (2006).
 - 20 Nurmalarani N, Yulizar Y, Apriandanu DOB, Bi₂O₃ nanoparticles: synthesis, characterizations, and photocatalytic activity, *IOP Conf. Ser.: Mater. Sci. Eng.* **763**(1), 012036 (2020).
 - 21 Sharma DK, et al., A review on ZnO: Fundamental properties and applications, *Mater. Today: Proc.* **49**, 3028–3035 (2022).
 - 22 Chitra M, et al., Band gap engineering in ZnO based nanocomposites, *Phys. E*. **119**, 113969 (2020).
 - 23 Dejene F, et al., Optical properties of ZnO nanoparticles synthesized by varying the sodium hydroxide to zinc acetate molar ratios using a Sol-Gel process, *Open Phys.* **9**(5), 1321–1326 (2011).
 - 24 Zhou J., Xu NS, Wang ZL, Dissolving behavior and stability of ZnO wires in biofluids: a study on biodegradability and biocompatibility of ZnO nanostructures, *Adv. Mater.* **18**(18), 2432–2435 (2006).
 - 25 Aboraia AM, et al., Tuning the structural as well as optical characteristics of ZIF-8 thin coatings through inclusion of reduced graphene oxide: a comparative study, *Opt. Quantum Electron.* **57**(1), 38 (2024).
 - 26 Davis E, Mott N, Conduction in non-crystalline systems V. Conductivity, optical absorption and photoconductivity in amorphous semiconductors, *Philos. Mag.* **22**(179), 0903–0922 (1970).
 - 27 Diab F, Ali I, Hassan A, Effect of successive plasma shots on the dielectric constant of the CdS: Mn thin films exposed to the helium electron beam of plasma focus device, *Sens. Actuators A*. **329**, 112819 (2021).
 - 28 Choudhury B, Choudhury A, Oxygen defect dependent variation of band gap, Urbach energy and luminescence property of anatase, anatase-rutile mixed phase and of rutile phases of TiO₂ nanoparticles, *Phys. E*. **56**, 364–371 (2014).
 - 29 Brahimi R, et al., Effect of S-doping toward the optical properties of WO₃ nanoparticles, *Mater. Chem. Phys.* **223**, 398–403 (2019).
 - 30 Diab F, Hassan AM, Influence of a plasma focus device on the structural and optical properties of highly conductive AZO thin films, *Mater. Today Commun.* **40**, 109856 (2024).
 - 31 Tauc J, Menth A, States in the gap, *J. Non-Cryst. Solids*. **8**, 569–585 (1972).
 - 32 Saha SK, et al., Effect of Co doping on structural, optical, electrical and thermal properties of nanostructured ZnO thin films, *J. Semicond.* **36**(3), 033004 (2015).
 - 33 Sharma R, et al., Reduced band gap & charge recombination rate in Se doped α -Bi₂O₃ leads to enhanced photoelectrochemical and photocatalytic performance: theoretical & experimental insight, *Int. J. Hydrogen Energy* **42**(32), 20638–20648 (2017).
 - 34 Afzal S, et al., Impact of transition metal doped bismuth oxide nanocomposites on the bandgap energy for photoanode application, *J. Nano Mater. Sci. Res.* **2**(1), 104–109 (2023).
 - 35 Zhukovsky M, et al., Dielectric, structural, optical and radiation shielding properties of newly synthesized CaO–SiO₂–Na₂O–Al₂O₃ glasses: experimental and theoretical investigations on impact of Tungsten (III) oxide, *Appl. Phys. A*. **128**(3), 205.
 - 36 Wemple SH, DiDomenico, M, Jr. Behavior of the electronic dielectric constant in covalent and ionic materials, *Phys. Rev. B*. **3**(4), 1338 (1971).
 - 37 Sahoo D, et al., In situ laser irradiation: the kinetics of the changes in the nonlinear/linear optical parameters of As₅₀Se₄₀Sb₁₀ thin films for photonic applications, *RSC Adv.* **11**(26), 16015–16025 (2021).
 - 38 Hassan AM, Alyousef HA, Zakaly HM, Optimizing the structure and optoelectronic properties of cuprite thin films via a plasma focus device as a solar cell absorber layer, *CrystEngComm*. **26**(11), 1590–1606 (2024).
 - 39 Mohamed HF, Abdel-Hady EE, Mohammed WM, Investigation of transport mechanism and nanostructure of Nylon-6, 6/PVA blend polymers, *Polymers* **15**(1), 107 (2022).
 - 40 Mohammed WM, et al., Nanostructure analysis and dielectric properties of PVA/sPTA proton exchange membrane for fuel cell applications: Positron lifetime study, *Radiat. Phys. Chem.* **208**, 110942 (2023).
 - 41 Alyousef HA, Hassan A, Zakaly HM, Reactive magnetron sputtered AlN thin films: structural, linear and nonlinear optical characteristics, *J. Mater. Sci.: Mater. Electron.* **34**(13), 1088 (2023).
 - 42 Rashad M, Darwish A, Blue shift of band gap for vanadyl 2, 3-naphthalocyanine (VONc) thin films monitored at thermal effect, *Mater. Res. Express.* **5**(2), 026402 (2018).
 - 43 Elsharkawy MR, Mohammed WM, Effect of the electric field on the free volume investigated from positron annihilation lifetime and dielectric properties of sulfonated PVC/PMMA, *Polym. Adv. Technol.* **35**(7), e6519 (2024).
 - 44 Zatsepin A, et al., Electronic structure and optical absorption in Gd-implanted silica glasses, *Phys. Status Solidi A* **216**(3), 1800522 (2019).
 - 45 Mohamed HF, et al., Study of mechanical and electrical properties through positron annihilation spectroscopy for ethylene-propylene-diene rubber biocomposites with treated wheat husk fibers, *Sci. Rep.* **14**(1), 24302 (2024).
 - 46 Mohammed WM, et al., Relationship between structural, electrical properties and positron annihilation parameters of V₂O₅-Cu₂O-P₂O₅ glasses, *Phys. B: Condens. Matter.* **694**, 416459 (2024).

- 47 Mohamed HF, et al., Investigation of the impact of an electric field on polymer electrolyte membranes for fuel cell applications, *Physics* **6**(4), 1345–1365 (2024).
- 48 Mohammed WM, et al., *Rheological behavior of PVC-based blends, IPNs, and gels, in Poly (vinyl chloride)-Based Blends, IPNs, and Gels* (Elsevier, 2024), pp. 255–280.
- 49 Ravi A, et al., Structural, morphological, optical and antibacterial performances of rare earth (Sm)-doped ZnO nanorods, *J. Rare Earths* **42**(11), 2119–2127 (2024).
- 50 Ali A, et al., Optical and dielectric results of $Y_{0.225}Sr_{0.775}CoO_{3\pm\delta}$ thin films studied by spectroscopic ellipsometry technique, *Results Phys.* **3**, 167–172 (2013).
- 51 Giri S, et al., Annealing-induced phase transformation in $In_{10}Se_{70}Te_{20}$ thin films and its structural, optical and morphological changes for optoelectronic applications, *RSC Adv.* **13**(36), 24955–24972 (2023).
- 52 Tholkappian R, Hamed F, Vishista K, Effect of annealing conditions on the struct-optical properties of $ZnFe_{1.96}La_{0.04}O_4$ nanoparticles, *Adv. Mater. Lett.* **7**(12), 971–978 (2016).
- 53 Parida A, et al., Influence of time dependent laser-irradiation for tuning the linear-nonlinear optical response of quaternary $Ag_{10}In_{15}S_{15}Se_{60}$ films for optoelectronic applications, *RSC Adv.* **13**(7), 4236–4248 (2023).
- 54 El-naggar A, et al., PVA/PVP/PEG polymeric blend loaded with nano- $Zn_{0.75-x}Fe_xCd_{0.25}S$: effect of iron concentration on the optical characteristics, *Appl. Phys. A.* **128**(3), 220 (2022).
- 55 Khenata R, et al., Elastic, electronic and optical properties of ZnS, ZnSe and ZnTe under pressure, *Comput. Mater. Sci.* **38**(1), 29–38 (2006).
- 56 Boyd R., *Contemporary nonlinear optics* (Academic Press, 2012).